

This document is the accepted manuscript version of the following article: Konstantinou, G., Kakkava, E., Hagelüken, L., Warriam Sasikumar, P. V., Wang, J., Makowska, M. G., ... Moser, C. (2020). Additive micro-manufacturing of crack-free PDCs by two-photon polymerization of a single, low-shrinkage preceramic resin. Additive Manufacturing, 101343 (28 pp.). <https://doi.org/10.1016/j.addma.2020.101343>

This manuscript version is made available under the CC-BY-NC-ND 4.0 license <http://creativecommons.org/licenses/by-nc-nd/4.0/>

## Additive micro-manufacturing of crack-free PDCs by two-photon polymerization of a single, low-shrinkage preceramic resin

Georgia Konstantinou<sup>a,\*</sup>, Eirini Kakkava<sup>b</sup>, Lorenz Hagelüken<sup>c</sup>, Pradeep Vallachira Warriam Sasikumar<sup>d</sup>, Jieping Wang<sup>a,b</sup>, Malgorzata Grazyna Makowska<sup>e</sup>, Gurdial Blugan<sup>d</sup>, Nikolaos Nianias<sup>a</sup>, Federica Marone<sup>f</sup>, Helena Van Swygenhoven<sup>e</sup>, Jürgen Brugger<sup>c</sup>, Demetri Psaltis<sup>b</sup> and Christophe Moser<sup>a</sup>

<sup>a</sup>École Polytechnique Fédérale de Lausanne, Laboratory of Applied Photonics Devices, STI IMT LAPD BM 4110, Station 17, CH-1015 Lausanne, Switzerland

<sup>b</sup>École Polytechnique Fédérale de Lausanne, Laboratory of Optics, CH-1015 Lausanne, Switzerland

<sup>c</sup>École Polytechnique Fédérale de Lausanne, Microsystems Laboratory 1, CH-1015 Lausanne, Switzerland

<sup>d</sup>EMPA, Laboratory of High Performance Ceramics, CH-8600 Dübendorf, Switzerland

<sup>e</sup>Paul Scherrer Institute, Photons for Engineering and Manufacturing, CH-5232 Villigen, PSI, Switzerland

<sup>f</sup>Paul Scherrer Institute, Swiss Light Source, CH-5232 Villigen, PSI, Switzerland

\*Correspondence to: [georgia.konstantinou@epfl.ch](mailto:georgia.konstantinou@epfl.ch)

### Abstract

Additive manufacturing (AM) methods are being integrated in ceramics fabrication either as the main manufacturing tool or for auxiliary purposes. By using polymers, powders and preceramic formulated materials, AM techniques are pushing towards higher resolution, lower shrinkage and shorter building time. Herein, we present the fabrication of ceramic microstructures ( $<200 \times 200 \times 200 \mu\text{m}^3$ ) with sub-micrometer resolution based on two-photon polymerization (TPP). 3D structuring of a preceramic resin by photopolymerization produces a so-called green body. The final ceramic part is obtained after pyrolysis of the green body. The high-resolution 3D shaped structures that we demonstrated could be employed as tools or components for microdevices. We report a lower linear shrinkage of 30% of TPP green bodies from a polysiloxane precursor with low porosity, no cracks and no significant shape distortion after pyrolysis, which implies the potential for highly controllable

manufacturing of micro-ceramic parts based on commercially available chemical compounds. The protocol for preparing, fabricating and developing the resin is detailed.

*Keywords:* additive manufacturing, 3D printing, polymer-derived ceramics, two-photon polymerization, preceramic polymers and two-photon lithography

2019 MSC: 00-01,99-00

---

## 1. Introduction

Additive manufacturing (AM) of complex shaped ceramic structures consists of several methods that are categorized mainly based on the feedstock and the material processing technique (optical, thermal, chemical etc.). For instance, Stereolithography (SLA), Digital Light Processing (DLP) and Inkjet Printing (IJP) use a slurry-based feedstock. Selective Laser Melting and Sintering (SLM/S) are powder-based techniques and Fused Deposition Modelling is used for solid-based raw materials [1-5]. AM technologies cover a wide range of feature resolution for the final sample, depending on the material, the size and the application of the 3D printed part. The resolution of the above techniques is lower for FDM and SLS/M (100–300  $\mu\text{m}$ ) and higher for SLA, IJP and DLP (25–100  $\mu\text{m}$ ). The highest resolution (100–200 nm) can be achieved using two-photon polymerization (TPP/2PP) technique [2,3].

The range of applications spans a variety of fields, such as the fabrication of devices for chemical or biological analysis (separation devices, high performance liquid chromatography or rRNA sequence analysis), for aerospace engineering (pumps and propulsion components, fans, gas turbines), electronics fabrication (transducers, RF ceramic capacitors), for automotive engineering (Piezo-ceramic components with ceramic substrates for sensors like anti-lock braking system (ABS) or traction control system (TCS/ASR systems), implant components or tools fabrication for biomedical applications (e.g. orthopedic or dental devices) [6-8].

For the production of micro-parts and micro-devices in general, light-based AM techniques can ensure high resolution when compared to other conventional AM technologies such as FDM. 3D AM based technologies have successfully

demonstrated the microfabrication of polymer derived ceramics (PDCs) based microcomponents [9-11]. In micro-stereolithography of preceramic polymers, the raw materials are based on liquid organosilicon polymers.

PDCs were first discovered in the 1960s [8] and new formulations are continuously being developed [4]. PDCs are synthesized through polymer-to-ceramic transformation of single source preceramic polymer precursors (PCPs). The microstructure and properties of final PDC ceramics can be tailored by changing the chemical composition of starting polymer precursors [12-13].

The silicon-containing preceramic polymers comprise various classes such as polysilazanes, polycarbosilanes, polyborosilanes, polysiloxanes etc. The difference between the classes of Si-polymers is related to the polymeric backbone structure; influencing the reactivity, the cross-linking behavior, the type of ceramic they convert to and correspondingly the properties of the final PDC [8]. This means that the molecular structure and the type of the preceramic polymer influence the composition, the number of phases and the phase distribution of the final ceramics, which implies variability of their overall resulting properties [14]. For instance, polyorganosilanes are composed of a Si-Si backbone and organic substituents attached to the silicon atoms [8]. The different side groups (substituents), such as alkyl, phenyl and metal alkoxide can be attached to the polymer backbone of the starting preceramic precursors, to improve the properties of the final PDC (e.g. magnetic, electrical, porosity, mechanical, energy storage capacity etc.).

In SLA printing of PCPs, the shaping is achieved by exposing the resin to UV irradiation. The resulting preceramic structure (green body) is afterwards converted into the final PDCs by pyrolysis under inert atmosphere [8]. The advances of high-power laser sources shifted the manufacturing techniques towards nonlinear processes for improving the final resolution of the polymer structure. TPP of various classes of preceramic polymers has shown to provide structures with resolution  $<200\text{nm}$  [9-10,14, 15-17]. This is due to the fact that non-linear effects in TPP lead to an excitation in a volume (voxel) better than the optical resolution.

In the work of Brigo et al. [9] a single preceramic polymer (polysiloxane) is used for the fabrication of microstructures by TPP and after pyrolysis at  $1000^{\circ}\text{C}$  a linear shrinkage  $>50\%$  was observed with no significant shape distortion. In the work of

Park et al. [15] and Wang et al [16], a different preceramic polymer which belongs to the class of polycarbosilanes in combination with an organometallic-type additive and/or silica nanoparticles as filler is used. Despite the versatile properties of the last one and the low-shrinkage observed after pyrolysis at 600° C, severe cracks are observed for temperatures higher than that. Lastly, Pham et al. [17] are using a type of polysilazane in purified argon atmosphere for similar purposes. At high pyrolysis temperatures they observe severe volume shrinkage and significant weight loss and densification.

In this paper, we demonstrate the fabrication of high-resolution (~350nm) polymer-derived ceramic microstructures through TPP of a highly viscous preceramic polymer, which belongs to a single class of PCPs, namely polysiloxanes without addition of any further substances (fillers or other additives). In general, polysiloxanes are inexpensive. Silicon oxycarbide ceramics derived from pyrolysis of polysiloxanes, show excellent chemical, electrical, physical, mechanical and biological properties [18-22]. Compared to polycarbosilanes and polysilazanes, polysiloxanes can often be used under ambient conditions, as they are chemically stable at room temperature. SPR-684 is a carbon-rich polysiloxane with methyl, vinyl and phenyl functionality. It is transparent in the visible and near infrared spectrum and yields a silicon oxycarbide ceramic after pyrolysis at 1000° C [12]. This term describes a chemical structure in which silicon is simultaneously bonded to carbon and oxygen, forming tetrahedral structural units of  $\text{SiO}_{4-x}\text{C}_x$  ( $x=1-4$ ) mixed bonds. These units build up an amorphous and heterogeneous Si-O-C network phase, in which free carbon might be dispersed and likewise  $\text{SiO}_2$ -enriched regions can form. After the pyrolysis, there is release of carbon-containing volatile units and this is the reason a decrease in the intensity for the C is usually observed. This class of preceramic resins also shows enhanced stability against crystallization and high-temperature resistance than originally anticipated [8,13-14].

The pyrolysis of preceramic structures was performed in a tubular furnace under argon atmosphere. As it was mentioned before, a linear shrinkage of 60%-70% of the TPP derived green body structure is usually reported after the pyrolysis step [9-10] and this is often improved by additives in the initial mixture [15-17]. We report in this paper a linear shrinkage of only 30% for a single preceramic polymer (no additives or

mixtures with other polymers), which shows low porosity, no cracks and no significant shape distortion. A large shrinkage can hinder detailed printing and deform the initial green body, which makes the resin formulation used in this work an attractive option.

In the following sections, we further elaborate on the fabrication of the preceramic resin, on the methods employed for TPP 3D printing and the developing protocol. The green bodies and the final pyrolysed ceramic structures are imaged by Bright Field (BF) and Scanning Electron Microscopy (SEM). They are chemically characterized by X-ray photoelectron spectroscopy analysis (XPS) and the final ceramic parts are additionally imaged by X-ray tomographic microscopy to provide structural information.

## **2. Materials and methods**

### *2.1 Experimental setup*

The experiments for the polymerization of the preceramic resins were conducted with the Nanoscribe Professional GT 3D printer. The laser source is an ultrafast erbium doped fiber laser system from Toptica Photonics AG, with central wavelength ( $\lambda$ ) at 780 nm, pulse width 100 fs, repetition rate 80 MHz, maximum output power 140 mW and peak power 25kW.

The oil-immersion configuration with a 63x objective lens (with numerical aperture NA 1.4) allowed avoiding aberrations. The maximum power delivered through this objective lens is 50mW. The photosensitive preceramic resin is deposited on a quartz slide (thickness: 170 $\mu$ m, refractive index: 1.55) for the printing process. Quartz slides are resistant to the pyrolysis temperature of 1000°C. The printing process is monitored through a camera installed in the 3D printer and by using the embedded bright field microscope. In Fig.1, a simplified sketch of the printing configuration is illustrated:

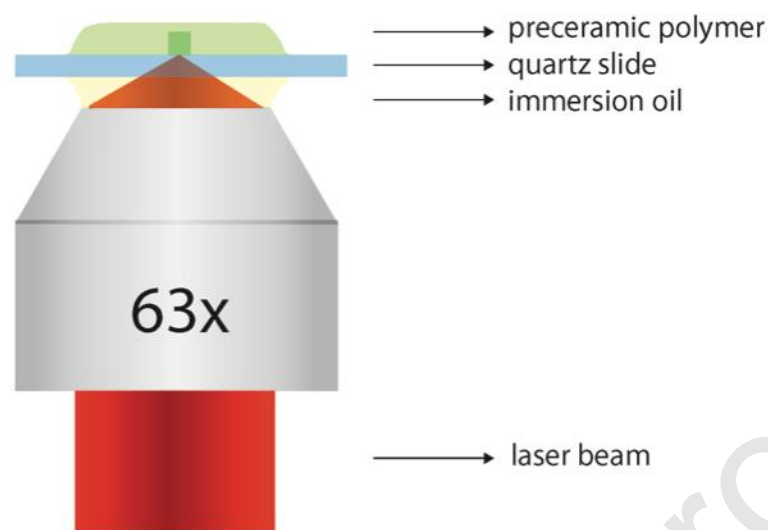


**Figure 1:** The oil-immersion printing configuration of the Nanoscribe 3D printer showing the printing of a cube starting from the top interface of the quartz slide. The fabrication is completed by bottom-up printing.

After the fabrication process with the Nanoscribe 3D printer, the unexposed preceramic polymer (PCP), which remains in liquid form, is removed via a chemical development with toluene. The quartz slide with the printed structures is dipped in toluene for 5 minutes. Finally, it is removed out of the toluene bath and the toluene left on the quartz slide gets evaporated.

The quartz slide with the green body microstructures is then placed in an alumina crucible and inserted into a tube furnace (STF 15/450, Carbolite Gero, Germany) for pyrolysis. The tube is purged with argon for 30 minutes and a low argon flow is maintained during pyrolysis. A heating/cooling rate of 5 K/min, a 2 h thermal crosslinking step at 200°C and 1 h dwell time at 1000°C is applied. An important reason for selecting this pyrolysis temperature is to achieve optimal polymer to ceramic conversion, which is verified by the detailed characterization of the prepared samples in the following paragraphs.

## 2.2 *Material formulation and polymerization mechanism*

Commercially available preceramic resins are widely used as single source precursors for synthesis of carbon rich SiOC ceramics [8-10]. The selected preceramic resin of this work is an inexpensive, commercially available polysiloxane (SPR-684, Polyramic series, Starfire Systems) with a refractive index higher than 1.5, which is close to the one of the quartz slide ( $n \sim 1.55$ ). This viscous single preceramic polymer is combined with 3.4% w/w concentration of a two-photon active photoinitiator (PI): 4,4'-bis(diethylamino) benzophenone (BDEBP) 99+% photoinitiator (ACROS ORGANICS) in order to prepare the final photosensitive mixture [3,12-13,23]. No additional fillers were used [15-17].

The preparation of the final formulation is divided in 4 steps: a) the PI is dissolved in acetone by using the magnetic stirring process at room temperature for  $\sim 6$  hours, b) the acetone-photoinitiator solution is mixed with the resin again by magnetic stirring (1:1 ratio) for  $\sim 9$  hours, c) while the magnetic stirring process continues, the resin solution is heated for 40 minutes on a hotplate set at  $\sim 50^\circ \text{C}$  and in this way the acetone is removed and d) the final resin is obtained after de-bubbling by vacuum drying for 30 minutes. As previously mentioned, polysiloxanes are easy to handle under ambient conditions, which makes their use versatile and cost-efficient by removing the need of an inert (moisture and oxygen-free) atmosphere ( $\text{N}_2/\text{Ar}$  glove box/ Schlenk line) [17], while it promotes repeatability in the production of customized ceramic parts.

The formation of the green body starts with two-photon absorption of the incoming light by the PI and the radical generation. Then, the polymerization is propagated via a vinyl polymerization mechanism [13]. Figure 2a shows the first step (initiation), where the double bond of the central oxygen breaks after two-photon absorption. Figure 2b illustrates the molecular structure of this polysiloxane and the propagation step via the cross linking mechanism of vinyl polymerization [13,14].

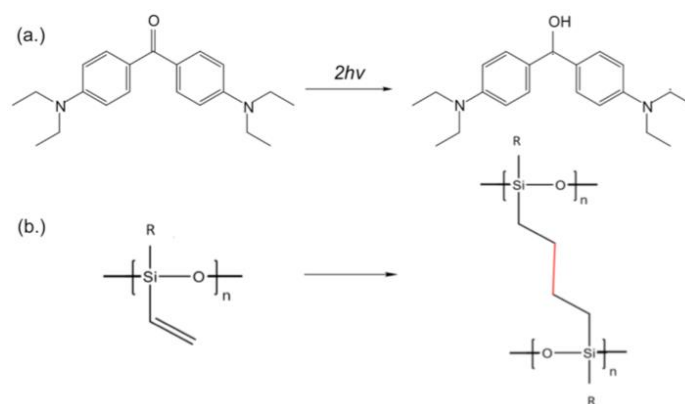


**Figure 2:** (a.) the free radical initiation step with two-photon absorption from the photoinitiator and (b.) the propagation step via vinyl polymerization.

At the second step, the propagation of the polymerization is accomplished via the vinyl polymerization. The first radical generated at the initiation step (photoinitiator) activates the radical polymerization of the participant monomer at the propagation step for the chain growth. The functional groups however do not participate in the crosslinking.

### 3. Results and Discussions

#### 3.1 Linewidth characterization and polymerization threshold

A standard printing configuration (63x objective lens) with  $NA=1.4$  (oil immersion) is used for high-resolution 3D structures with an optical lateral resolution of 280nm based on the Abbe diffraction limit:

$$d = \frac{\lambda}{2NA} \quad (1)$$

In order to characterize the dependence of the printed linewidth on the light exposure dose and investigate the polymerization threshold for a single layer exposure, we scanned in galvo-scanning mode a set of 15 lines with 6 different power levels from 5 to 30 mW. Each line, of 10  $\mu\text{m}$  length, is exposed on a single pass and attaches to the slide. The scanning speed ranges from 0.05  $\mu\text{m/s}$  to 10  $\mu\text{m/s}$ . Fig. 3a



shows the images of the printed lines obtained with a Differential Interference Microscope (DIC) corresponding to the 6 different power levels used. In each image of Fig. 3a, the scanning speed is increasing from left to right. We measured the linewidth (FWHM) of each line for all power levels before the chemical development of the sample since the lines are collapsing after dipping into in toluene. In Figure 3b, the linewidth is plotted as a function of the scanning speed for all the power levels in a 2D plot.

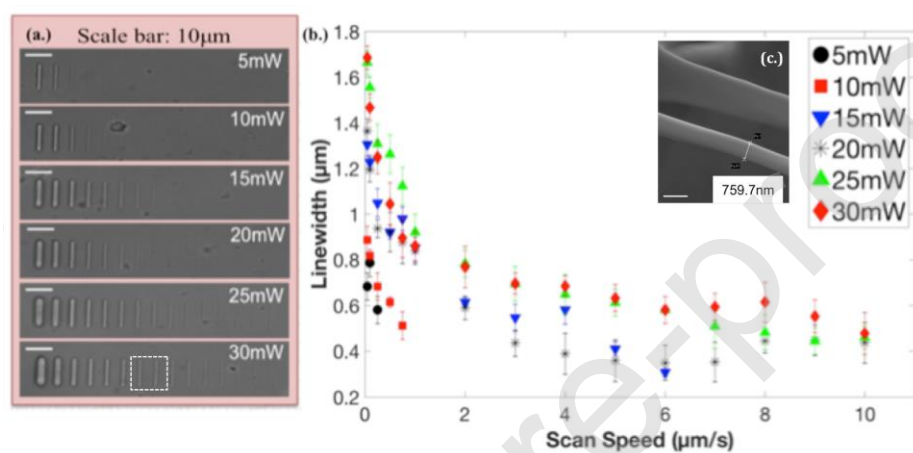


**Figure 3:** (a.) The 15 lines for each power level are presented. The scale bar is 10 μm. The 7<sup>th</sup> and 8<sup>th</sup> line (for power level 30mW) are highlighted with a white, dashed-line square for Fig.3.c, (b.) The measured line widths (FWHM) are plotted with the error bars and with different shape/color for each power level. (c.) SEM image of the two lines highlighted in (a.), the sample is tilted at 45°. The scale bar is 1 μm.

In Fig. 3.b, we can observe that the minimum measured linewidth is ~349nm (blue triangle with average power 15mW and scan speed 6 μm/s). The linewidth exponential decay versus the scan speed curve is related to the exponential decay of monomer concentration upon light exposure [3,24-25]. By applying the TPP exposure dose formula, we calculate the minimum TPP dose, which results in an efficient and distinct line printing based on the DIC image shown in Fig. 3a, [24-29]. The polymerization threshold corresponds to a dose of 8.5-9.9 J/cm<sup>2</sup> for writing a line on a single layer. Additionally, for higher power and higher scanning speed values we can observe saturation for the linewidth with negligible differences for the three highest

power levels used. The energy per pulse is correspondingly calculated to be 0.125nJ and the formula used for the TPP dose is [28,29]:

$$D = f_{rep} \tau_L \sqrt{\frac{2}{\pi}} \frac{P_t}{w_0 v} \quad (2)$$

where  $f_{rep}$  is the repetition rate of the laser,  $\tau_L$  is the pulse duration,  $v$  represents the scanning speed,  $w_0$  is the lateral resolution of the focal spot and  $P_t$  is the average power. In Figure 3.c, two lines printed with different scanning speeds (2  $\mu\text{m/s}$  and 3  $\mu\text{m/s}$ ) at 30mW power level, are imaged -after development- by Scanning Electron Microscopy, when the sample is tilted at 45°, in order to demonstrate an assessment of the cross sectional view. Two printed cubes were used to support these lines in order to avoid collapsing during the chemical development or adhesion issues with the quartz slide. Stress forces from these cubes to the lines apply after pyrolysis and for this reason no data for pyrolysed lines are presented. The linewidth characterization is not a direct indication of the dose required for the fabrication of 3D microstructures. This study only gives us the minimum feature size we can expect in a 3D structure. For this purpose, a set of dose tests with cuboids took place in the same 3D-printing system.

### 3.2 Shape fidelity evaluation with cuboid microstructures

Cuboid microstructures were printed with scanning speeds between 400 and 8000  $\mu\text{m/s}$  (more than 40 times higher than the maximum speed used for single lines in paragraph 3.1) and an average power of 25 mW, which corresponds to a peak intensity of 3.95 TW/cm<sup>2</sup>. The slicing and hatching distance (100 nm or 200 nm) along with the cumulative dose resulted in the building of a solid 3D structure. The dose tests are in the range 9.31 to 186.18 mJ/cm<sup>2</sup> [28-29].

The optical spot size is defined by the optical properties of the writing system concerning the lateral optical resolution (1) and axial optical resolution ( $\lambda/\text{NA}^2$ ). The final cured voxel size though –above the threshold energy- depends on the dose. However, in the case of 3D printed structures the overlap between consecutive lines and layers results in a cumulative energy deposition around each voxel and therefore

the dose needed for the TPP of the whole volume of the structure is significantly lower than those reported for a single line in the previous section. The fidelity of the structure and the characteristics of the cured 3D volume depend on several parameters such as the linewidth, the layer thickness (both are dose dependent), the scanning pitch, also called hatching distance (x and y) and the layer pitch, also called slicing distance (layer-by-layer distance). All these will affect the gradual accumulation of the dose and determine the successful adhesion between the exposed areas [30]. The scheme in Fig. 4 illustrates the writing of a 3D structure and the dose tests that lead to success or failure. A set of cubes was printed employing different combinations of the above parameters in order to determine the optimal printing protocol and furthermore to study its effect on the final structure quality (Fig.4.c) [31-32].

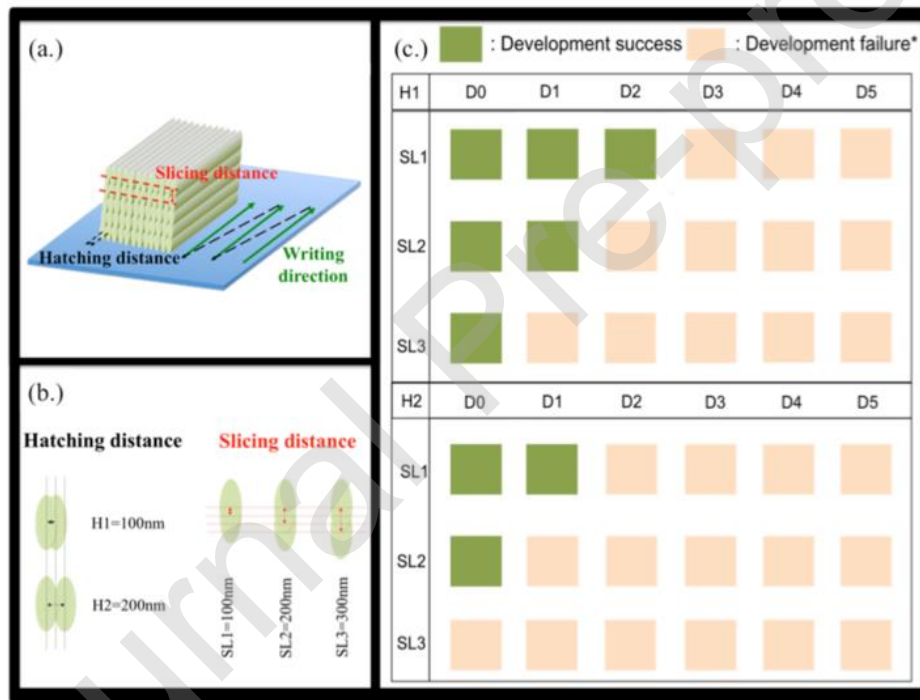


**Figure 4:** (a.) 3D illustration of the writing of a cuboid structure. The green arrows illustrate the writing direction of the scanned line whereas the dashed black arrows show how the writing will be continued for the next line (b.) The hatching is related to the lateral overlap of the voxels on a single layer and the slicing is the layer distance. Both are shown with 2D illustration for all tested values, (c.) Table with Success vs Failure after development for a set of 36 cubes printed with different parameters (dose

from  $D0=186.18 \text{ mJ/cm}^2$  to  $D5=9.31 \text{ mJ/cm}^2$ ). \*Development failure: partial or complete.

The parameters that were varied are: a) the hatching distance, b) the slicing distance and c) the exposure dose from D0 to D5 ( $D0=186.18 \text{ mJ/cm}^2$ ,  $D1=106.39 \text{ mJ/cm}^2$ ,  $D2=62.06 \text{ mJ/cm}^2$ ,  $D3=37.24 \text{ mJ/cm}^2$ ,  $D4=18.618 \text{ mJ/cm}^2$  and  $D5=9.31 \text{ mJ/cm}^2$ ). This test took place in order to evaluate the optimal conditions that ensure high fidelity of the final solid 3D structure. The criteria for selecting the optimized conditions were based on the characteristics of the resulting structures such as the roughness, the shrinkage and the porosity after pyrolysis. The set of cubes is first printed and monitored in real time in the Nanoscribe system through the integrated bright field microscope. All cubes were fabricated with support structures (cylindrical pillars) in order to minimize the stress forces at the interface between the substrate and the cube that would possibly result in severe sample deformations during the next steps. Then, the printed green bodies are dipped in toluene bath for 5 minutes. This step, which we also name here chemical development, is a critical step concerning the success or failure of the fabrication of the desired structure.

After this step, we deposit a 20nm gold layer (DP650, Alliance Concept, France) on the samples to collect Scanning Electron Microscope images. The pink-colored rectangles (Fig.5) represent two examples of cubes that collapsed partially after the development (Fig.5. a, b, e, f) while the green rectangles represent the ones that were successfully developed (Fig.5. c, d, g, h).

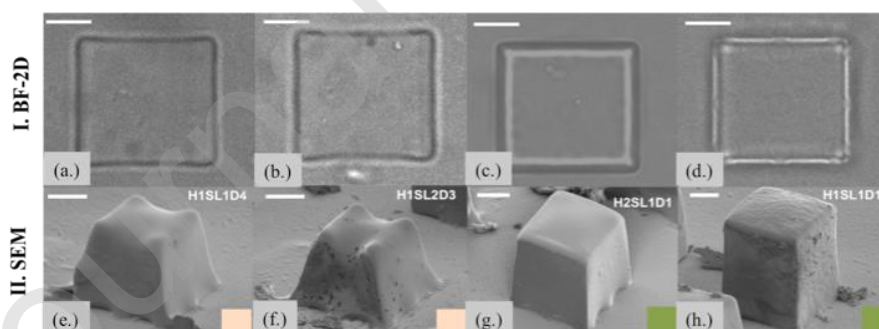


**Figure 5:** I. Bright field images of four different cubes obtained with the Nanoscribe BF microscope, right after the end of the printing process (before toluene bath). II. SEM images of the same cubes after the chemical development (green bodies). Scale bars:  $10 \mu\text{m}$ .

Figure 6 presents the experimental points of the linewidth tests versus the dose. The expected linewidth for the cubes printed with good fidelity was obtained by extrapolation for the mentioned dose range (D0, D1 and D2 resulted in solid cubes-green colored squares).

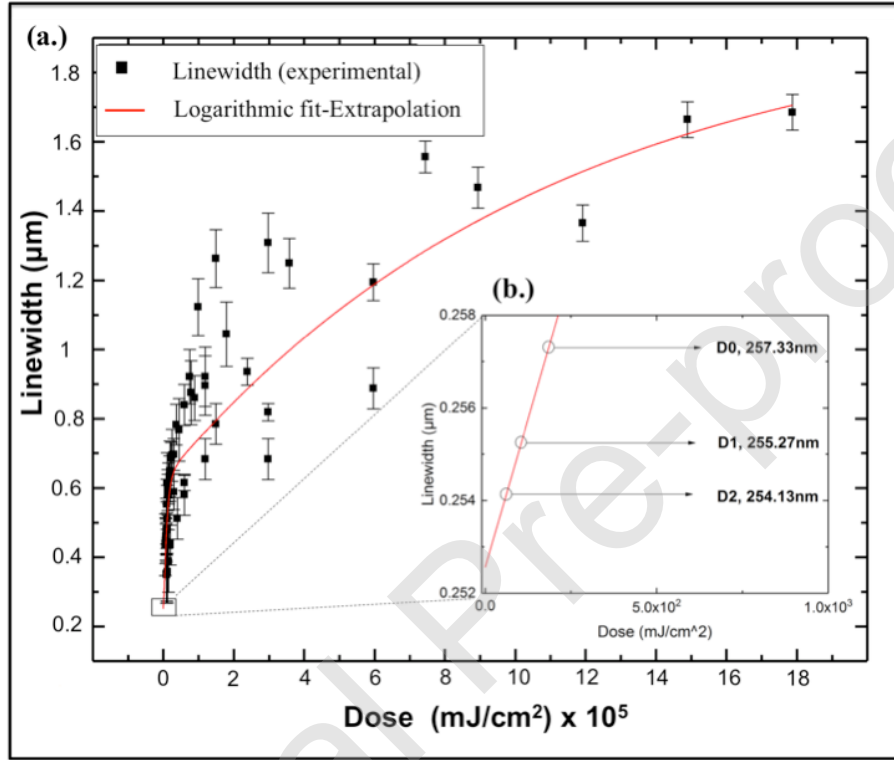


**Figure 6:** (a.) Dependence of the linewidth on the exposure dose, (b.) By extrapolation, the dose used for the fabrication of the cubes (small square) is zoomed in and presented in the same graph.

Based on the extrapolated values of the linewidth for the dose values used for the successful fabrication of the solid cuboids, we obtain values of linewidth below the minimum linewidth (350nm) measured in the case of the single-line printed samples. This result is expected because we used a dose  $\sim 53$  times lower than the threshold dose for the exposure of a line on a single layer. The proper selection of the hatching

and slicing distance and the cumulative dose will result in a subset of solid cubes with good fidelity.

Based on the observations above (Figure 5 and Figure 6), we selected the subset of cubes that ensure solid, non-collapsed structures after the development procedure as the best candidates for the inert gas pyrolysis. The subset of cuboids, which was imaged by SEM before pyrolysis and for which some samples were presented in Figure 5, was not the one inserted into the pyrolysis furnace. New cuboids with identical printing parameters to the aforementioned ones were printed a second time in order to be inserted into the furnace for pyrolysis without Au coating on their surface. The two sets of cuboids were at first inspected under a DIC microscope to verify that their shapes are the same and ensure that the final comparison is valid. In addition, by separating the cuboids after development from the cuboids that are additionally pyrolysed, we remove the effect of Au coating on the pyrolysis step, which could affect the final ceramic part. In the 3D design of the cuboids, nine pillars were also included and were symmetrically located under the bottom layer of the cuboid structures in order to promote adhesion and reduce the deformation because of the stress between the printed structure and the substrate.

The selected cuboid green bodies are converted into SiOC by 1000° C thermal treatment (as described in details in paragraph 2.1). In order to quantify the mean linear shrinkage of these cubes, SEM images of the pyrolysed and Au-coated parts were also collected. Figure 7 shows the resulting pyrolysed ceramic cubes. One sample of the green body with successful development is shown in order to show the comparison with the sintered ones. We measured an isotropic shrinkage after pyrolysis with a mean value of linear shrinkage between 32% and 38%. This value is lower than what is commonly found in preceramic polymers (60-70%) and shown for TPP fabricated microstructures until now [9-10]. This is attributed to the low and approximately constant coefficient of thermal expansion of the resin over a broad temperature range along with the high viscosity of the material [12]. The slight differences of the shrinkage between the top and bottom parts of the cube are attributed to the stress forces of the supporting pillars to the bulk solid cuboid structure. This result underlines the high potential of the material for controlled fabrication of ceramic components even in the micron scale.

	Col.1 (0°)	SEM	Col.2 (60°)	Col.3: Shrinkage	Col.4: AFM	Col.5: $R_a$ (nm)
Green body	(1.1)		(1.2)	—	—	—
Ceramic	(a.1)		(a.2)	32%	(a.3)	65.2
	(b.1)		(b.2)	34%	(b.3)	96.3
	(c.1)		(c.2)	38%	(c.3)	47.4
	(d.1)		(d.2)	36%	(d.3)	54.6

**Figure 7:** SEM and AFM images (Col.1,2 and 4) of ceramic cubes printed with different parameters, the corresponding mean values of the linear shrinkage (Col.3) and the average roughness (Col.5) measured with Nanoscope analysis of the Atomic Force Microscope. Scale bar: 10  $\mu\text{m}$ .

Further measurements to determine the average roughness of the fabricated cuboids shown in Figure 7, were conducted on an area of 4  $\mu\text{m}$  x by 4  $\mu\text{m}$  by using the Bruker's FastScan ScanAsyst Atomic Force Microscope system. The range of average roughness, presented in the Col.5 of Figure 7, is a bit higher than expected for two-photon fabrication structures (Nanoscribe: minimum surface roughness  $R_a \leq 20\text{nm}$ ) because of the pyrolysis process. The reason is that the different printing parameters (a, b and c) affect the shrinkage percentage and correspondingly the quality of adhesion between the scanned lines and layers. Moreover, the internal structure of the cuboids after pyrolysis was investigated by performing X-ray tomographic microscopy at the TOMCAT synchrotron beamline of the Swiss Light Source (SLS). The tomographic scans were performed using a standard detector setup for full field

tomography composed of a scintillator, an optical microscope with magnification 40x and a camera, which provides a field of view  $0.3 \times 0.4 \text{ mm}^2$  with  $0.1625 \mu\text{m}$  pixel size. The energy of the used X-ray beam was 20 keV. 1501 projections were acquired over 180 deg with 200 ms exposure time per projection. Figures 8a and 8b present the results of the tomographic studies after pyrolysis for the structures printed with the same conditions as the green bodies shown in Fig. 8e and Fig. 8f. Figures 8c and 8d of the tomographic results show the tomography reconstruction corresponding to the successfully developed and pyrolysed cuboid structures printed with the same parameters as the green bodies shown in SEM results in Fig.8g and Fig.8h.

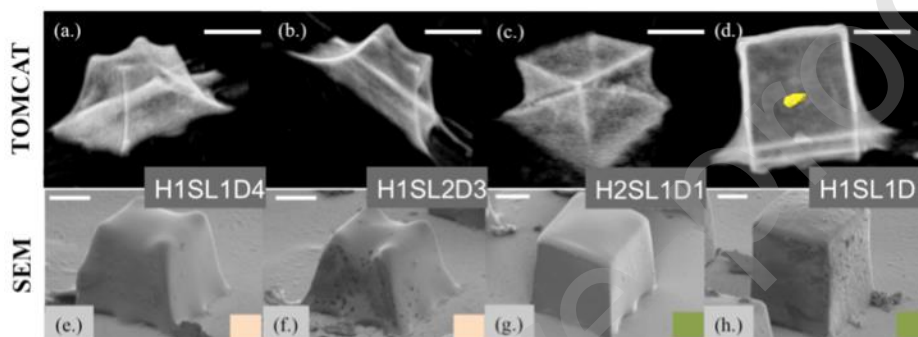


**Figure 8:** Volume rendering of tomographic data (TOMCAT) for the pyrolysed cubes shown in reference to the green bodies (SEM). Scale bar:  $10 \mu\text{m}$

Tomographic studies revealed that in most cases, the volume of the printed cubes was homogeneous and crack-free and only in a few cases, the presence of closed pores was observed, which is illustrated by the yellow feature in Figure 8.d of the tomographic results. Both Figures 7 and 8 show the deformation and change of shape of the cubes for different printing parameters. The presented studies lead to the conclusion that the printing conditions resulting in a solid, low-shrinkage, pore-free and smooth structure, are H1SL1 and H2SL1 within a dose range from D0 to D1. For these conditions, the porosity is expressed as the volume fraction of the pores and was found in the range from 0 to 1.3‰ compared to one magnitude larger for the collapsed structures.

Figure 9 presents the bar-plot illustrating the effect of the printing parameters used for the samples in Figure 7 on the linear shrinkage and the average roughness. The



configurations with the minimum shrinkage are selected for fabricating complex structures. We show in this graph the isotropic shrinkage [33, 34] that was mentioned previously (L: Length, W: Width and H: Height of the cubes).

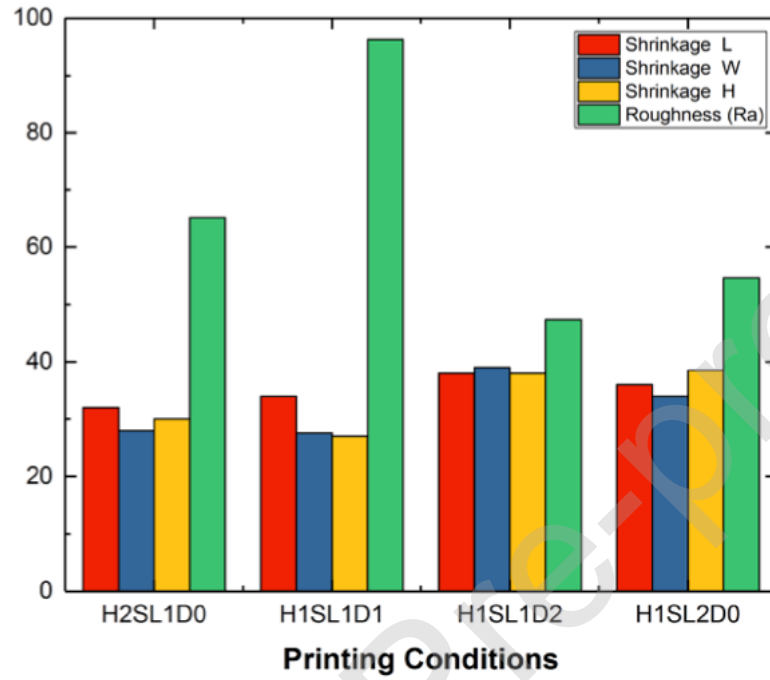


**Figure 9:** The linear shrinkage percentage and the average roughness  $R_a$  evaluated for the four best printing conditions.

### 3.3 XPS analysis

The pyrolytic transformation of the preceramic resin to the final ceramic is examined by X-ray photoelectron spectroscopy (XPS) using the PHI VersaProbe II scanning XPS microprobe (Physical Instruments AG). Both the green and ceramic parts were analysed and the corresponding spectra are presented in Figure 10.

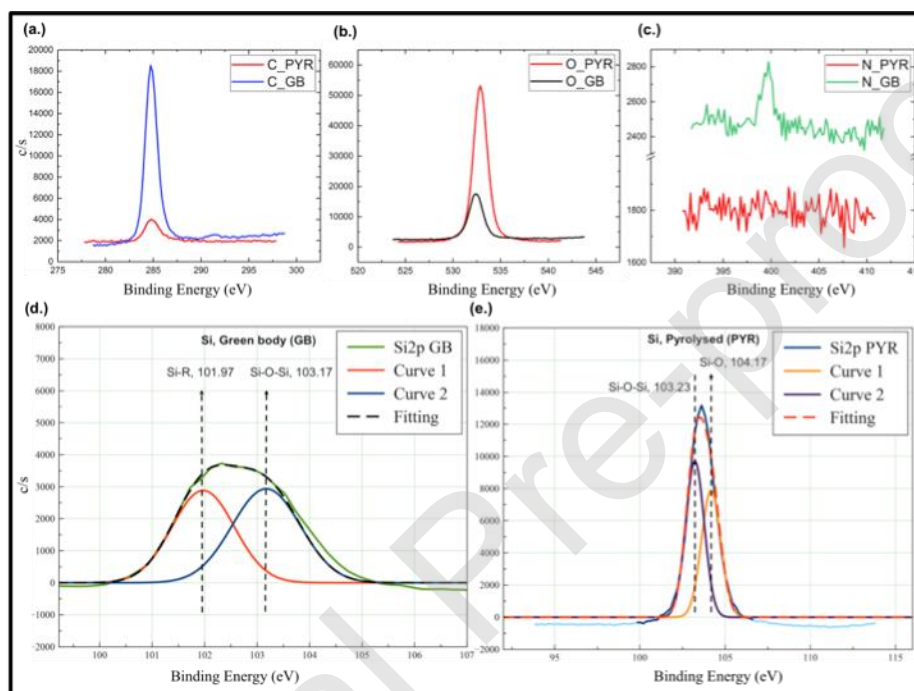


**Figure 10:** (a.) XPS data of the C1s bond in both states (green body and pyrolysed ceramic), (b.) XPS data of the O1s, (c.) XPS data of the N1s (d.) XPS in the Si2p region of the green body, (e.) XPS in the Si2p region of the pyrolysed part.

XPS spectra demonstrate the presence of Si, C and O atoms in both green body and final ceramic. The presence of C is confirmed by the existence of C1s peak in the XPS spectra. In Fig. 10.a, a decrease in intensity of C1s is observed for the sample after pyrolysis. This is attributed to the release of carbon containing volatile units during polymer to ceramic conversion [14]. The oxygen peak can be observed in both states (Fig. 10.b). The difference of the binding energy of the oxygen in the SiO<sub>2</sub> and

in the organic compounds is negligible, approximately 0.2 eV [35]. From the O1s peak we can identify the percentile amount of oxygen, which is higher in the pyrolysed state. The reason for this large amount of oxygen in the pyrolysed state may be attributed to the presence of small amount of O<sub>2</sub> –which is always expected- inside the tubular furnace during the pyrolysis step. The effect of that oxygen amount can be significantly higher for a microstructure compared to several larger ceramic structures (e.g. discs). In macroscale, the relative amount would be negligible because the oxygen for both cases (micro- and macro-scale) would diffuse mostly homogeneously [36,37]. A peak representing nitrogen (Fig. 10.c) can be seen at ~400 eV in the preceramic state, which is mainly attributed to the presence of residual photoinitiator.

In the Si2p region, the two fitted peaks of the green body are assigned to the presence of Si-O and Si-C bonds within the polymer backbone (Fig.10d). The structure of the starting polymer precursor mainly comprises of Si-O-Si units in the polymer backbone along with methyl, vinyl and phenyl functional groups. In the deconvoluted Si2p spectra of the green body, the peak at ~101.97 eV represents the Si-R bonds and the second peak at ~103 eV corresponds to the Si-O bonds from the polymer backbone [38- 39]. The Si2p spectrum of the pyrolysed part (Fig.10e) has mainly two bands at 103.23 eV and 104.17 eV representing Si-O-Si units and Si-O bonds from the amorphous SiO<sub>2</sub> units in the final ceramics. The presence of SiO<sub>2</sub> signal leads to the shifting of the fitted curve to higher binding energy levels. In the following table the percentile elemental composition is presented for both states and confirms the aforementioned results [38-41].

Table 1: Elemental composition of the green state and the ceramic state

State	C1s (%)	N1s (%)	O1s (%)	Si2p (%)
Green Body	57.05	0.94	26.26	15.75
Polymer Derived Ceramic	6.94	0.36	64.12	28.58

A significant increase in the percentile amount of Si and O is observed in the pyrolysed sample and a corresponding decrease in the carbon content, advocating to the fact that the PDC is obtained after pyrolysis. In conclusion, the XPS results validate that the low shrinkage occurs from the effectiveness of the pyrolysis process.

### 3.4 Complex 3D microstructures

Based on the obtained results, the laser scanning parameters were optimized, which allowed fabricating complex pyrolysed ceramic 3D microstructures with good fidelity. Figure 11 presents the CAD previews of a chess rook, a dragon and a micro-nozzle and the final pyrolysed part imaged by SEM. The printing time of the chess rook (dimensions:  $50\mu\text{m} \times 50\mu\text{m} \times 60\mu\text{m}$ ) was 1 h 50 mins and the printing time of a dragon with dimensions more than double of the chess rook was  $\sim 2\text{h}$ . However, there was some difficulty in reproducing the finer features of the micro-dragon. Additionally, since the tail and wings are thin and without any support structures, they moved during the pyrolysis process.

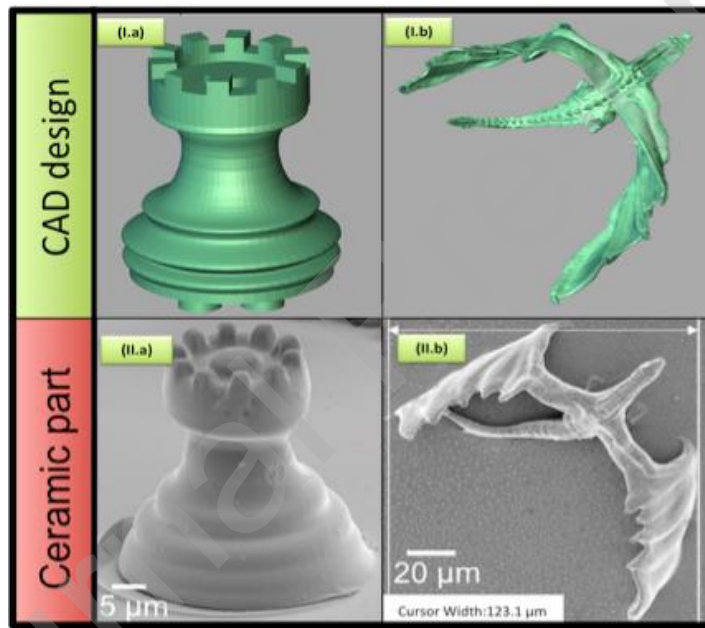


**Figure 11:** I. The CAD designs of two different structures (Describe © provided by Nanoscribe), II. the final pyrolysed parts.

Finally, Figure 12 shows the fabricated micro-nozzle tip with 2D cross sections.

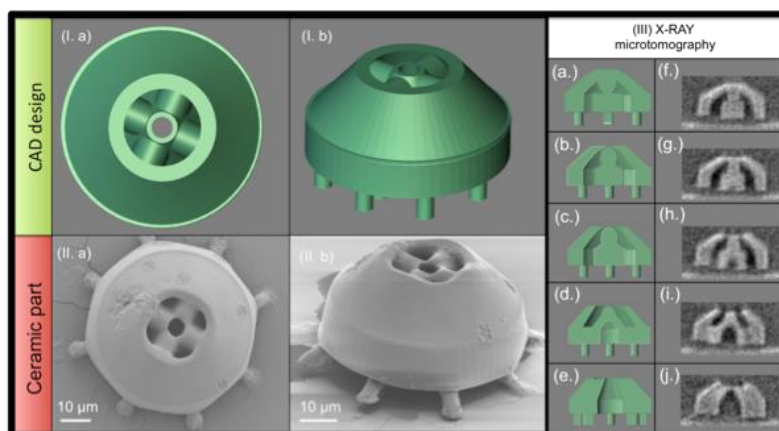


**Figure 12:** The CAD design (I.a and I.b) of the nozzle compared with the final pyrolysed part (II.a and II.b) and SEM images at 0° and 60°. In III(a-j), X-ray microtomographic sections of the nozzle are presented and compared with the illustrated cross sections of the nozzle.

Figure 12.II.b reveals that some support structures were detached from the quartz substrate. The printing time of the nozzle tip (dimensions: 85  $\mu\text{m}$  x 85  $\mu\text{m}$  x 50  $\mu\text{m}$ ) was  $\sim$ 4 h 30mins. In this part, it was necessary to have a thick outer and inner nozzle ( $\sim$ 5  $\mu\text{m}$  each) tube to avoid collapsing of the structure. By X-Ray micro-tomography with 0.7  $\mu\text{m}$  resolution, we confirmed with the Fig.12 (III.) that the fabricated internal capillaries ( $\sim$ 6-8  $\mu\text{m}$ ) did not collapse or block after development or pyrolysis. To our knowledge, this nozzle is the first two-photon fabricated ceramic microstructure where high aspect ratio capillaries survived after development and pyrolysis. Since SiOC ceramics are well known for their mechanical properties and resistance in harsh environments [8], the micro-nozzle tip can be considered as a promising candidate for microdroplets delivery for low viscosity liquids.

#### 4. Conclusion

In this work we investigated the polymerization parameters of a commercially available polysiloxane resin, which was prepared in combination with a two-photon active photoinitiator and 3D printed with Nanoscribe Professional GT 3D printer. The printed green body was then developed and pyrolysed in inert atmosphere up to 1000°C to yield silicon oxycarbide ceramic microstructures ( $<200 \times 200 \times 200 \mu\text{m}^3$ ). We

observe an isotropic shrinkage with a linear shrinkage value between 32-38% which implies high-controllable ceramics manufacturing. This low shrinkage is attributed to the molecular structure of this preceramic polymer, which results in extensive crosslinking and leads to high ceramic yield. By optimizing the fidelity of prints using an appropriate combination of exposure dose, hatching and slicing distance, the porosity fraction of these ceramic structures was found very low as demonstrated after synchrotron tomographic imaging and the roughness measured by Atomic Force Microscopy is found to be <100 nm for the final ceramic parts. Based on the results obtained from the test cuboid structures, a specific printing configuration was selected for the fabrication of complex 3D structures and finally a micro-nozzle tip was printed and pyrolysed successfully.

Until now, mostly scaffolds or photonic crystal microstructures have been printed with two-photon polymerization of PCPs and the mentioned linear shrinkage was >50%. We showed that ceramic microstructures which can find applications in several fields can be fabricated. As shown, a ceramic-based micro-nozzle for micro-droplets delivery or micro-manipulation can be realized and provide high robustness and chemical resistance due to the specific properties of ceramics if compared to other materials such as polymers.

#### **Declaration of interests**

The authors declare that they have no known competing financial interests or personal relationships that could have appeared to influence the work reported in this paper.

#### **Acknowledgements**

This work was supported by Strategic Focus Area (SFA)- Advanced Manufacturing for the Ceramic X.0 –High-precision micro-manufacturing of ceramics.

We would like to acknowledge the Paul Scherrer Institut, Villigen, Switzerland for provision of synchrotron radiation beamtime at the TOMCAT beamline of the Swiss Light Source.

Finally, we acknowledge Mr. Dorsaz, responsible for the Nanoscribe 3D printer at the CMI facility of EPFL, Mr. Mettraux, responsible for the Surface Characterization lab and X-ray Photoelectron Spectroscopy system at the Materials Department of EPFL and Mr. Perrenoud, responsible for the PIXE platform at the Civil Engineering Institute of EPFL.

## References

- [1] Zocca, A., Colombo, P., Gomes, C. M., & Günster, J. (2015). Additive manufacturing of ceramics: issues, potentialities, and opportunities. *Journal of the American Ceramic Society*, 98(7), 1983-2001.
- [2] Chen, Zhangwei, et al. "3D printing of ceramics: a review." *Journal of the European Ceramic Society* (2018).
- [3] Maruo, S., Nakamura, O., & Kawata, S. (1997). Three-dimensional microfabrication with two-photon-absorbed photopolymerization. *Optics letters*, 22(2), 132-134.
- [4] Eckel, Zak C., Chaoyin Zhou, John H. Martin, Alan J. Jacobsen, William B. Carter, and Tobias A. Schaedler. "Additive manufacturing of polymer-derived ceramics." *Science* 351, no. 6268 (2016): 58-62.
- [5] Sachs, Emanuel, Michael Cima, and James Cornie. "Three dimensional printing: rapid tooling and prototypes directly from CAD representation." 1990 International Solid Freeform Fabrication Symposium. 1990.
- [6] Galante, Raquel, Celio G. Figueiredo-Pina, and Ana Paula Serro. "Additive manufacturing of ceramics for dental applications: A review." *Dental Materials* (2019).

- [7] Mitic, Vojislav V., et al. "Fractal frontiers in microelectronic ceramic materials." *Ceramics International* 45.7 (2019): 9679-9685.
- [8] Colombo, Paolo, et al. "Polymer derived ceramics: 40 years of research and innovation in advanced ceramics." *Journal of the American Ceramic Society* 93.7 (2010): 1805-1837.
- [9] Brigo, L., Schmidt, J. E. M., Gandin, A., Michieli, N., Colombo, P., & Brusatin, G. (2018). 3D Nanofabrication of SiOC Ceramic Structures. *Advanced Science*, 5(12), 1800937.
- [10] Gailevičius, D., Padolskytė, V., Mikoliūnaitė, L., Šakirzanovas, S., Juodkasis, S., & Malinauskas, M. (2019). Additive-manufacturing of 3D glass-ceramics down to nanoscale resolution. *Nanoscale Horizons*, 4(3), 647-651.
- [11] Vyatskikh, Andrey, et al. "Additive manufacturing of titanium dioxide for dielectric photonic crystals." *Advanced Fabrication Technologies for Micro/Nano Optics and Photonics XII*. Vol. 10930. International Society for Optics and Photonics, 2019.
- [12] <https://www.starfiresystems.com/wp-content/uploads/2018/03/Polyramic-Overview.pdf>
- [13] Ionescu, Emanuel. "Polymer-Derived Ceramics." *Ceramics science and technology* (2011): 457-500.
- [14] Mera, G., Navrotsky, A., Sen, S., Kleebe, H. J., & Riedel, R. (2013). Polymer-derived SiCN and SiOC ceramics—structure and energetics at the nanoscale. *Journal of Materials Chemistry A*, 1(12), 3826-3836.
- [15] Park, S., Lee, D. H., Ryoo, H. I., Lim, T. W., Yang, D. Y., & Kim, D. P. (2009). Fabrication of three-dimensional SiC ceramic microstructures with near-zero shrinkage via dual crosslinking induced stereolithography. *Chemical Communications*, (32), 4880-4882.
- [16] Wang, X., Schmidt, F., Hanaor, D., Kamm, P. H., Li, S., & Gurlo, A. (2019). Additive manufacturing of ceramics from preceramic polymers: A versatile



- stereolithographic approach assisted by thiol-ene click chemistry. *Additive Manufacturing*, 27, 80-90.
- [17] Pham, T. A., Kim, D. P., Lim, T. W., Park, S. H., Yang, D. Y., & Lee, K. S. (2006). Three- dimensional SiCN ceramic microstructures via nano- stereolithography of inorganic polymer photoresists. *Advanced Functional Materials*, 16(9), 1235-1241.
- [18] Bansal, N. P., & Boccaccini, A. R. (Eds.). (2012). *Ceramics and composites processing methods*. John Wiley & Sons.
- [19] Martínez-Crespiera, S., Ionescu, E., Kleebe, H. J., & Riedel, R. (2011). Pressureless synthesis of fully dense and crack-free SiOC bulk ceramics via photo-crosslinking and pyrolysis of a polysiloxane. *Journal of the European Ceramic Society*, 31(5), 913-919.
- [20] Bauer, J., Crook, C., Izard, A. G., Eckel, Z. C., Ruvalcaba, N., Schaedler, T. A., & Valdevit, L. (2019). Additive Manufacturing of Ductile, Ultrastrong Polymer-Derived Nanoceramics. *Matter*, 1(6), 1547-1556.
- [21] Crook, C., Bauer, J., Izard, A. G., de Oliveira, C. S., e Silva, J. M. D. S., Berger, J. B., & Valdevit, L. (2020). Plate-nanolattices at the theoretical limit of stiffness and strength. *Nature Communications*, 11(1), 1-11.
- [22] Vallachira Warriam Sasikumar, P., Mueller, E., Clement, P., Jang, J., Kakkava, E., Panusa, G., ... & Blugan, G. (2020). In vitro Cytocompatibility Assessment of Ti-modified Silicon-oxycarbide Based Polymer-derived Ceramic Implantable Electrodes under Pacing Conditions. *ACS Applied Materials & Interfaces*.
- [23] Haq, B. S., Khan, H. U., Alam, K., Ajmal, M., Attaullah, S., & Zari, I. (2015). Determination of two-photon absorption cross sections of photosensitizers and its implications for two-photon polymerization. *Applied optics*, 54(1), 132-140.

- [24] Morales-Delgado, E. E., Urio, L., Conkey, D. B., Stasio, N., Psaltis, D., & Moser, C. (2017). Three-dimensional microfabrication through a multimode optical fiber. *Optics express*, 25(6), 7031-7045.
- [25] Flory, P. J. (1953). *Principles of polymer chemistry*. Cornell University Press.
- [26] Mueller, J. B., Fischer, J., Mayer, F., Kadic, M., & Wegener, M. (2014). Polymerization Kinetics in Three- Dimensional Direct Laser Writing. *Advanced Materials*, 26(38), 6566-6571.
- [27] Delrot, Paul, Damien Loterie, Demetri Psaltis, and Christophe Moser. "Single-photon three-dimensional microfabrication through a multimode optical fiber." *Optics express* 26, no. 2 (2018): 1766-1778.
- [28] Oakdale, J. S., Ye, J., Smith, W. L., & Biener, J. (2016). Post-print UV curing method for improving the mechanical properties of prototypes derived from two-photon lithography. *Optics express*, 24(24), 27077-27086.
- [29] Cardenas-Benitez, B., Eschenbaum, C., Mager, D., Korvink, J. G., Madou, M. J., Lemmer, U., Martinez-Chapa, S. O. (2019). Pyrolysis-induced shrinking of three-dimensional structures fabricated by two-photon polymerization: experiment and theoretical model. *Microsystems & Nanoengineering*, 5(1), 1-13.
- [30] Zheng, X., Cheng, K., Zhou, X., Lin, J., & Jing, X. (2018). An adaptive direct slicing method based on tilted voxel of two-photon polymerization. *The International Journal of Advanced Manufacturing Technology*, 96(1-4), 521-530.
- [31] Park, S. H., Lee, S. H., Yang, D. Y., Kong, H. J., & Lee, K. S. (2005). Subregional slicing method to increase three-dimensional nanofabrication efficiency in two-photon polymerization. *Applied Physics Letters*, 87(15), 154108.

- [32] Kim, Jong Min, and Hiroshi Muramatsu. "Two-photon photopolymerized tips for adhesion-free scanning-probe microscopy." *Nano letters* 5, no. 2 (2005): 309-314.
- [33] You, Shangting, Pengrui Wang, Jacob Schimelman, Henry H. Hwang, and Shaochen Chen. "High-fidelity 3D printing using flashing photopolymerization." *Additive Manufacturing* 30 (2019): 100834.
- [34] Tian, X., Li, D., Chen, Z., & Zhou, W. (2012). Study on the fabrication accuracy of ceramic parts by direct stereolithography. *Virtual and Physical Prototyping*, 7(3), 195-202.
- [35] Moulder, John F. "Handbook of X-ray photoelectron spectroscopy." *Physical electronics* (1995): 230-232.
- [36] Kaspar, J., Graczyk-Zajac, M., & Riedel, R. (2012). Carbon-rich SiOC anodes for lithium-ion batteries: Part II. Role of thermal cross-linking. *Solid State Ionics*, 225, 527-531.
- [37] Martínez-Crespiera, S., Ionescu, E., Schlosser, M., Flittner, K., Mistura, G., Riedel, R., & Schlaak, H. F. (2011). Fabrication of silicon oxycarbide-based microcomponents via photolithographic and soft lithography approaches. *Sensors and Actuators A: Physical*, 169(1), 242-249.
- [38] Yu, S., Tu, R., & Goto, T. (2016). Preparation of SiOC nanocomposite films by laser chemical vapor deposition. *Journal of the European Ceramic Society*, 36(3), 403-409.
- [39] Ryan, J. V., & Pantano, C. G. (2007). Synthesis and characterization of inorganic silicon oxycarbide glass thin films by reactive rf-magnetron sputtering. *Journal of Vacuum Science & Technology A: Vacuum, Surfaces, and Films*, 25(1), 153-159.
- [40] Vashisth, Aniruddh, et al. "Mechanical size effects of amorphous polymer-derived ceramics at the nanoscale: experiments and ReaxFF simulations." *Nanoscale* 11.15 (2019): 7447-7456.

- [41] Sorarù, Gian Domenico, et al. "Chemical durability of silicon oxycarbide glasses." *Journal of the American Ceramic Society* 85.6 (2002): 1529-1536.